

# CFD BASED OPTIMIZATION OF HIGH-LIFT DEVICES USING A MESH MORPHING TECHNIQUE

Ricardo G. Silva<sup>†</sup>, Alexandre P. Antunes<sup>\*</sup>, Ricardo B. Flatschart<sup>\*</sup>, João L. F. Azevedo<sup>‡</sup>  
<sup>†</sup> Universidade de São Paulo, São Paulo, SP, Brazil

<sup>\*</sup> Embraer, Research and Development Branch, São José dos Campos, SP, Brazil

<sup>‡</sup> Instituto de Aeronáutica e Espaço, São José dos Campos, SP, Brazil

**Keywords:** *CFD, High-Lift Configuration, Aerodynamic Design, Morphing Mesh*

## Abstract

*The present work explores the benefits of the mesh morphing methodology to perform two-dimensional aerodynamic studies over a high-lift configuration. The studies are conducted with the mid-span section of the Trapezoidal Wing model, which is a model developed by NASA to provide a database for CFD validation. Here, the mesh morphing methodology is employed in order to support two sets of studies that contemplate the displacements of the flap panel. The mesh morphing methodology allows the displacements of the flap panel without incurring into the need to regenerate the mesh. The numerical simulations are accomplished using the Reynolds-averaged Navier Stokes equations and the Spalart-Allmaras turbulence model. In the present case, a freestream Mach number of 0.15 and a Reynolds number of 9.0 million, based on the model mean aerodynamic chord, are the imposed flight conditions.*

## 1 Introduction

High-lift devices play an important role in the aircraft take-off and landing performance [1], thus, justifying the importance and the required attention to be invested in the design of such components. The two main streams of the aerodynamic design of these devices are the geometrical shape and the relative positioning among each element. In the design process, wherein shape modifica-

tions are being carried out, it is mandatory that the cruise configuration of the wing should not be changed by the design process, unless the design process of the high-lift devices is being performed in a coupled fashion with the cruise configuration.

The limitation, regarding the impossibility of violating the cruise shape, imposes a few constraints in the shape design of the high-lift devices. Firstly, it yields a restriction in the modification the slat component. Secondly, it is important to guarantee that the leading edge of the flap components lies inside the confined region limited by the cruise shape. In the present work, two sets of studies are conducted with the mid-span section of the Trapezoidal Wing configuration [2, 3]. The selected geometry of interest consists in configuration nine from the Trap Wing model [2, 3], which is characterized by presenting a slat and flap deflections of 30 deg. and 25 deg., respectively, with a partial span flap. The first study consists in the optimization of the flap positioning by means of a framework created inside the modeFRONTIER software. In this particular case, the optimization is focused on achieving the best lift-over-drag ratio. In the second study case, a systematic parametric variation of the flap panel positioning is performed to obtain the maximum lift coefficient,  $C_{l_{max}}$ . Afterwards, the flap positioning that yields the maximum lift coefficient is evaluated considering a three-dimensional analysis.

## 2 Configuration and Meshes

The idea is to take advantage of the available experimental data from the NASA Trap Wing in order to latter perform comparisons with the obtained numerical results from the optimization process and the parametric study. Thereby, a three-dimensional numerical analysis is initially performed for configuration nine of the Trap Wing. Figure 1 shows an overview of the high-lift components that constitute configuration nine.



**Fig. 1** NASA wind tunnel and the configuration nine of the trapezoidal wing model.

The meshes for the numerical simulations are generated with the ICEM-CFD mesh generator [4]. In the mesh generation process, a hybrid approach that combines tetrahedral and prismatic elements is employed. Figures 2 and 3 show some details about the surface mesh generated over configuration nine. In the mesh generation process, special attention is focused on the leading edge of the respective high-lift components in order to guarantee that the prismatic layer yields a  $y^+$  of one, or less, for the first cell off the wall. The final volumetric mesh has a total of 26 million cells.

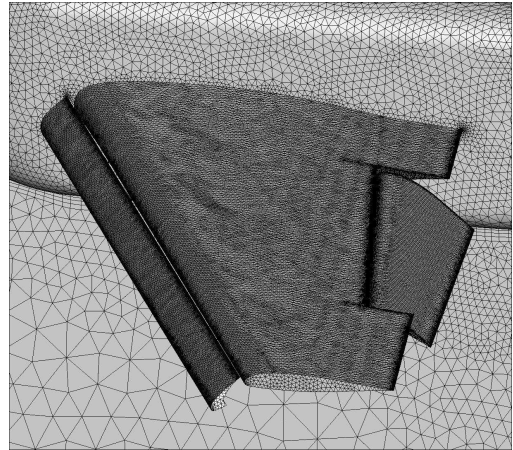


**Fig. 2** Details of the surface mesh generated over the configuration nine of the Trap Wing - Side View.

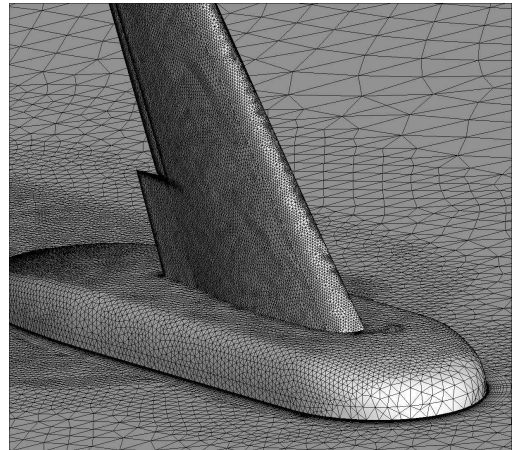


**Fig. 3** Details of the surface mesh generated over the configuration nine of the Trap Wing - Front View.

## 3 Preliminary 3-D Calculations

Numerical simulations, considering the RANS formulation with the Spalart-Allmaras turbulence model [5], are performed with the CFD++ commercial package [6] for configuration nine of the Trap Wing. These initial simulations are conducted in order to verify how good is the agreement of the numerical simulations with regard to the experimental results. It is worth to remember that the study on the parametric variation of the flap positioning will later update the three-

dimensional geometry in order to evaluate the improvements in the maximum lift coefficient,  $C_{L_{max}}$ , of the reference model. Thereby, the capability of adequately reproducing the original experimental results is an important aspect in order to obtain confidence on the simulations performed with the modified configuration.

Figure 4 shows the comparison between the experimental results and the numerical ones for configuration nine in terms of the lift coefficient as a function of the angle of attack. It is possible to observe that, although there are quite considerable differences between uncorrected and corrected experimental results, the present calculations do agree fairly well with the corrected experimental data. It is worth mentioning that the experimental data correction is only available up to the stall angle of attack. However, here, the correction available for the linear region was extrapolated in order to allow the use of the experimental data up to the stall region.

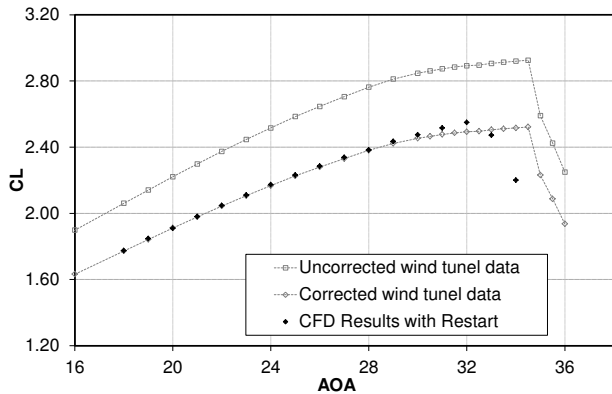


**Fig. 4** Comparison between the experimental and the numerical results for configuration nine.

It can be observed that the numerical results are capturing the angular coefficient of the curve and the maximum lift coefficient. However, stall in the computational results is occurring 3 deg. sooner than in the experimental data obtained with the imposed extrapolated correction. The numerical simulations are always performed considering the results obtained from the previous angle of attack calculation as a starting condition for the current angle of attack.

Figure 5 shows pressure coefficient,  $C_p$ , contours superimposed on shear lines over configuration nine for an angle of attack of 32 deg. The flow pattern represents configuration nine at its maximum lift condition. One can notice that there is a considerable detached region near the trailing edge of the wing-fuselage junction. However, this detached region seems to be self-contained in this region of the model and it does not propagate towards the wing outboard sections.

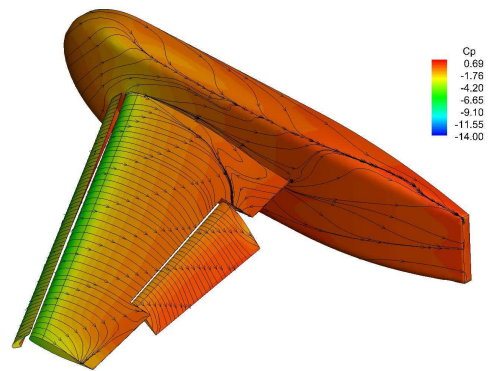


**Fig. 5** Pressure coefficient contours and the shear lines for configuration nine at 32 deg. angle of attack.

#### 4 Two-Dimensional Optimization Process

The mid-span section of the Trap Wing configuration nine is taken as the starting point in the optimization study. In Fig. 6, one can observe the respective components that comprise this mid-span section. Moreover, Fig. 6 also indicates the initial positioning of the flap panel.

The optimization workflow is implemented in the modeFRONTIER [7] software and Fig. 7 provides an overview of the created environment. In this figure, the green boxes show the input files that are connected to an appropriate code that executes some computation and the blue boxes represent the output from the computations. Basically, the created environment bridges the solver setup, the mesh morphing procedure, the numerical simulation and the post-processing of the results. The optimization algorithm is responsible

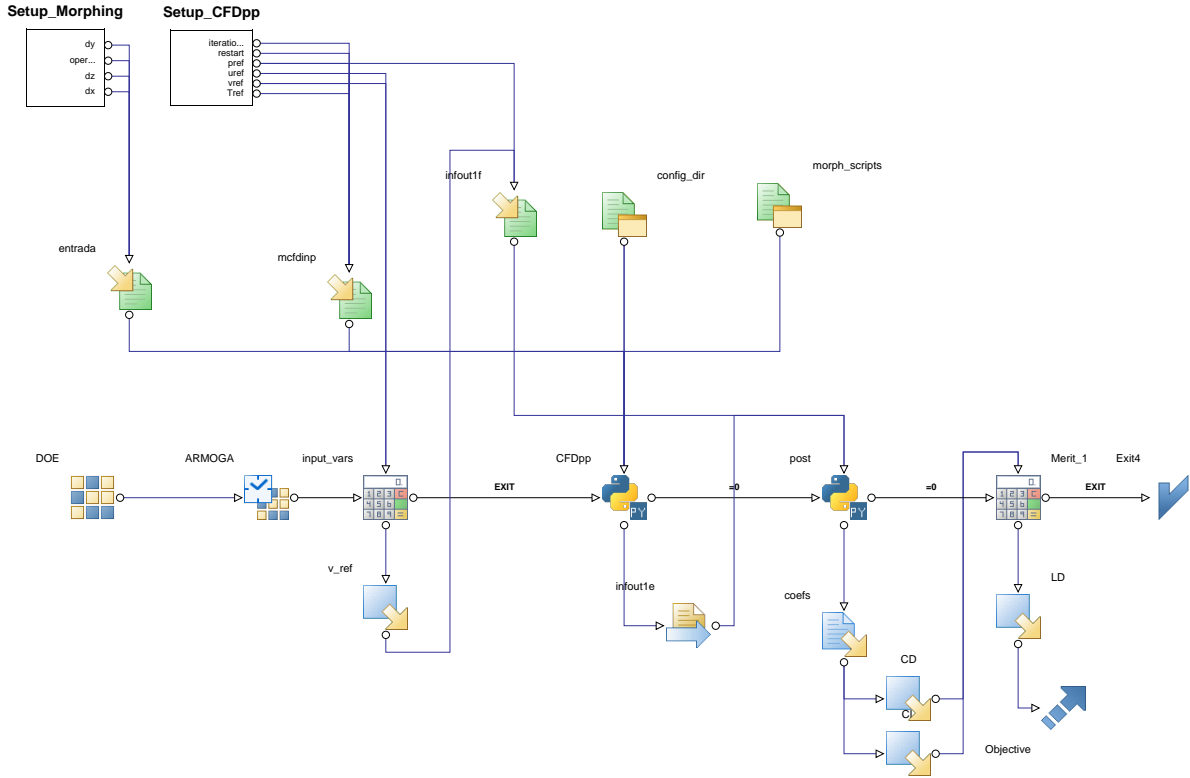


Fig. 7 Optimization workflow implemented in modeFRONTIER.

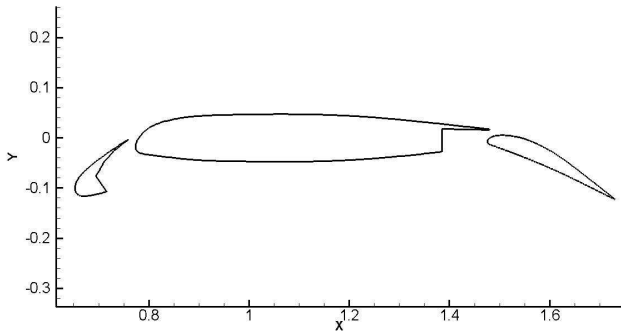


Fig. 6 High-lift components from the mid-span section of configuration nine.

to close the loop in the search of the best configuration that satisfies the optimization requirements.

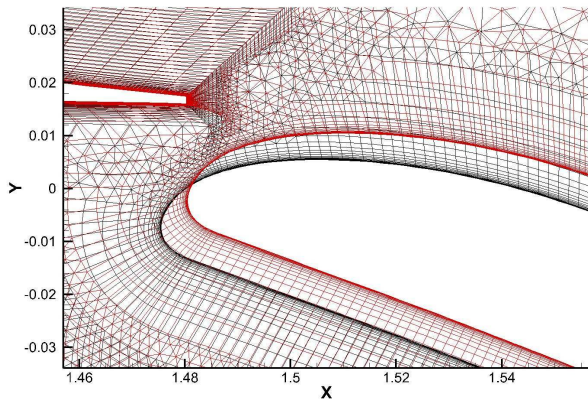
The optimization statement is defined as

$$\begin{cases} \max & L/D \\ \text{w.r.t.} & dx, dy \text{ displacements} \\ \text{subjected to} & AoA = 30 \\ \text{subjected to} & M_\infty = 0.15, \text{ and } Re = 9.0 \times 10^6. \end{cases}$$

where  $dx$  and  $dy$  are the displacements imposed on the flap position by the optimization algorithm. The decision to adopt the  $L/D$  as the merit function was focused on driving the optimization process towards solutions that would minimize detached flow regions. This approach is an alternative to avoid the imposition of constraints in the optimization process.

In this search for the best flap positioning, the mesh morphing methodology is employed for two main reasons. The first one is related to the possibility of avoiding the generation of the entire mesh every time a new positioning is analyzed. The second reason lies on the fact that mesh morphing maintains a reasonable portion of

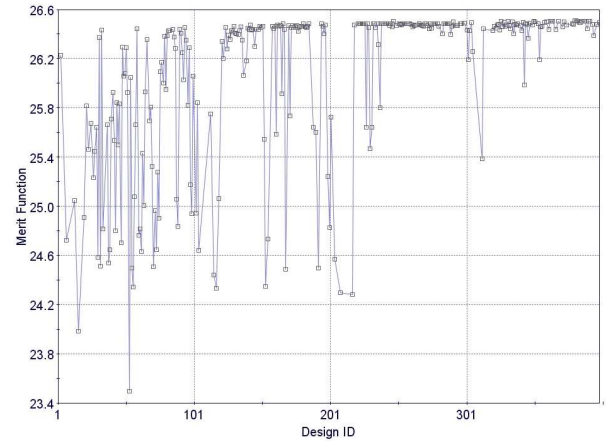
the mesh unaltered, which minimizes the effect of the mesh over the obtained aerodynamic coefficients. Figure 8 shows mesh details for two distinct positions of the flap panel. It can be noticed that, in regions far from the boundary for which modifications are imposed, the meshes are almost identical and, therefore, accomplishing the desired result.



**Fig. 8** Mesh morphing methodology employed in the optimization studies.

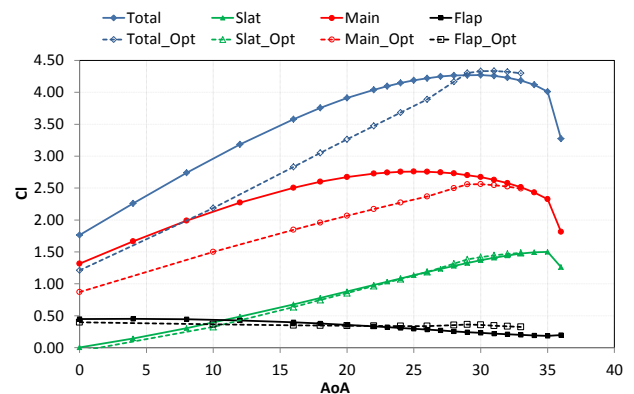
Figure 9 shows the convergence history during the optimization process. The increase in the value of the objective function, as function of the successive evaluated individuals, can be clearly seen in the figure. The optimization is performed by the use of the ARMOGA genetic algorithm [8] with the following setup: population size of 20 individuals, mutation probability of 1.5% and number of generations equal to 20. During each of the analysis runs of optimization process, a total amount of 1,000 iterations are considered in the numerical simulations with the CFD++ code. This adopted number of iterations is sufficient to have a residue drop between 4 and 5 orders of magnitude, which is a good trade-off between the computational cost and convergence of the aerodynamic coefficients.

Figure 10 shows the comparison between the  $C_l$  versus angle of attack curve for each component from both high-lift device configurations, *i.e.*, the baseline and the optimized ones. It is interesting to notice that there is a considerable



**Fig. 9** The convergence history towards the optimum flap positioning.

decrease in  $C_{l0}$  for the optimized configuration with respect to the baseline. Actually, throughout most of the angle of attack range studied, the optimized configuration has lower  $C_l$  than the baseline one. The optimized configuration only shows improvements, in terms of the lift coefficient, for values of angle of attack above 30 deg. At 32 deg., there is an increase of 0.09 in the maximum lift coefficient for the optimized configuration.



**Fig. 10** Comparison between the  $C_l$  versus angle of attack curves for the baseline and the optimum configuration.

## 5 Parametric Flap Positioning Study

This section presents the results obtained with the parametric displacement of the flap panel. In Fig. 11, it is possible to observe the maximum lift coefficient,  $C_{l_{max}}$ , for different positions of the flap panel. The baseline configuration is also represented in this  $C_{l_{max}}$  map by the  $x$  and  $y$  values equal to (0,0). The best position is given by  $x = 0.0250$ ,  $y = -0.0150$  and this information is adopted to move the three-dimensional flap panel of configuration nine.

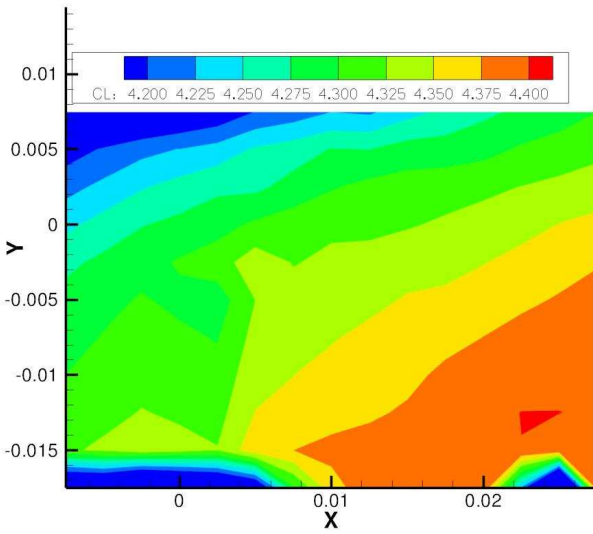


**Fig. 11** Maximum lift coefficient for each of the parametric positioning of the flap component.

Figure 12 shows the  $C_l$  versus angle of attack curve for the best configuration previously identified by the parametric analysis. One can observe that there is an increase in the total lift coefficient for angles of attack above 27 deg. in comparison with the reference configuration. The increase in the lift coefficient is provided by the flap panel, since the slat and the main element components have, for different angles of attack, a lower or at most an equal lift coefficient value than those observed for the reference (baseline) configuration. The stall occurs at 30 deg. and there is an increase in  $C_{l_{max}}$  of 0.13 with respect to the baseline value.

The optimum flap position for  $C_{l_{max}}$  leads to a reduction on  $C_{l_0}$ . Figure 13 shows the Mach

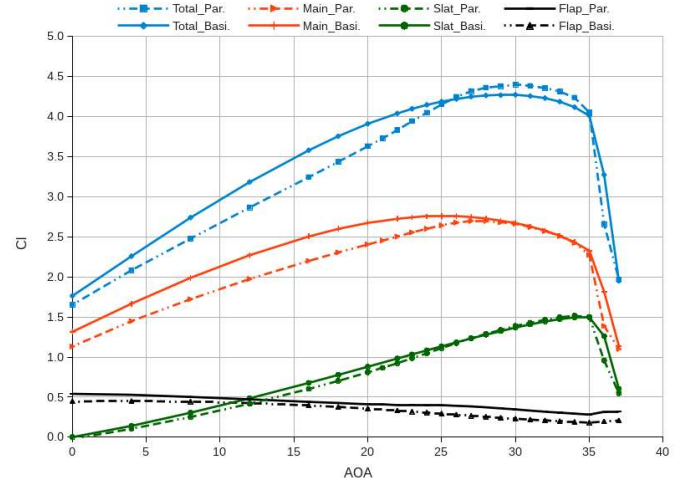


**Fig. 12** Comparison between the  $C_l$  versus angle of attack curve for the baseline and the optimum configuration obtained via parametric optimization.

number contours for the baseline configuration, on the right side, and for the optimum configuration, on the left side. The trailing edge of the

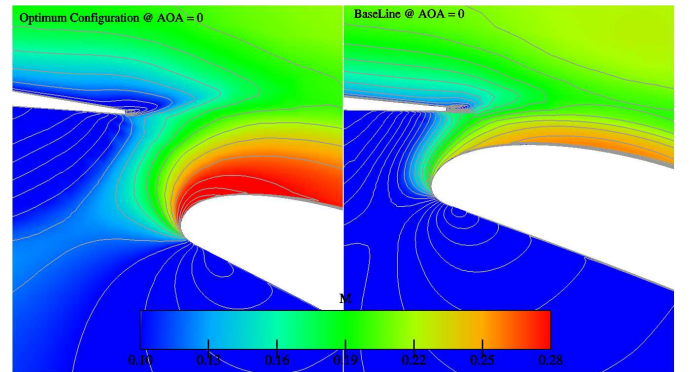


**Fig. 13** Mach number contours of flow around baseline and the optimum configuration obtained via parametric optimization.

main element presents higher velocity levels for the baseline configuration than those observed for the optimized configuration. Higher velocity levels yield a relief in the pressure rise imposed on the boundary layer, thus alleviating separation problems or permitting increased lift coefficient [9]. This phenomena is know as “dumping” effect and it explains the reason of having

a lower lift coefficient for the optimized configuration. This influence by which the flap affects the main element pressure distributions can be clearly seen in the pressure distribution shown in Figure 14. In this figure, the red symbols in-

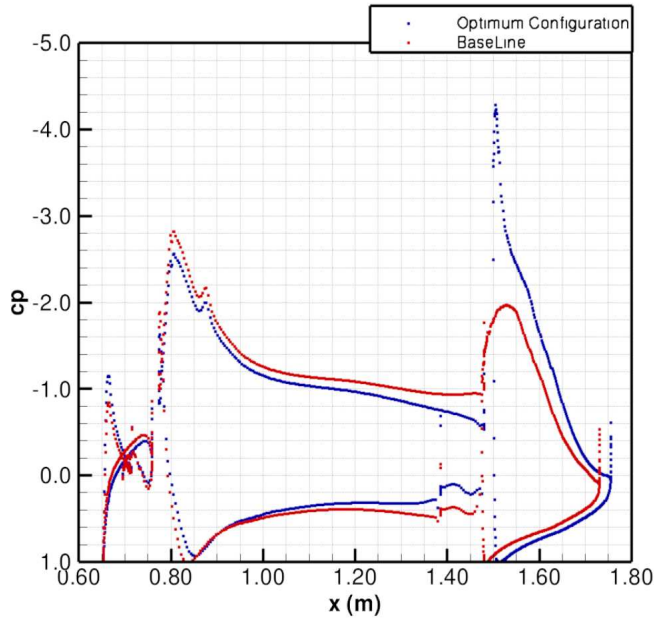


**Fig. 14** Comparison between pressure coefficient ( $c_p$ ) from baseline and optimum configuration.

dicates the baseline pressure coefficient distributions, whereas the blue symbols represent the optimized configuration results.

Figure 15 shows that, for most of the evaluated angles of attack, the flap panel presents a detached region near its trailing edge. The extension of this separated region increases as the angle of attack is increased from 0 to 20 deg. It is only for angles of attack larger than 20 deg. that the separated region begins to decrease. The flow becomes fully attached at the rear part of flap panel only at 30 deg. angle of attack, which is precisely the angle of attack for which the flap has been optimized.

The literature [10] shows that a single slotted flap configuration, that is primarily designed to extract the utmost maximum lift coefficient, will usually have the flow characteristics shown in Fig. 15. The flap component has a tendency of presenting a detached region at lower angles

of attack. The flow over the flap panel becomes attached only in the angle of attack range close to the value of  $\alpha$  that yields the maximum lift coefficient. Figure 16 is extracted from Ref. [10] and it shows that there are three aerodynamic design types for the high-lift devices. The one that provides the highest maximum lift coefficient, type B, has this characteristic of having a detached flow at lower angles of attack, as our simulations have shown.

## 6 Semi-Empirical Methodology

In this section, a semi-empirical methodology known as the critical section approach is presented as an alternative for the three-dimensional numerical simulations. Here, the method used to optimize the wing consists in defining the maximum lift coefficient based on two sets of information. The first one consists in the wing loading distribution that comes from a three-dimensional inviscid analysis. The viscous two-dimensional numerical simulations, from a few wing sections, provide the complementary data that allows the use of the method.

The semi-empirical approach does not capture the three-dimensional effects that are of great importance in the determination of the maximum lift coefficient. In the considered methodology, the maximum lift coefficient is obtained whenever the loading curve reaches a maximum local (section) lift coefficient,  $C_{l_{max}}$ , as shown in Figure 17. The red points represent the maximum lift coefficient for the baseline configuration at the station 1.07 and 1.87 meters. The blue point is the  $C_{l_{max}}$  obtained for the optimum configuration defined by the parametric study. Here, it is worth to mention that it is assumed that the maximum  $C_l$  occurs in the flapped region of the wing. Therefore, only the mid-span station is being considered in the present analysis.

In order to take into account the three-dimensional effects, a correction factor is created to provide a more realistic estimation of the maximum lift coefficient. This correction factor is generated considering the baseline configuration and the obtained value is 0.69. The estimates of

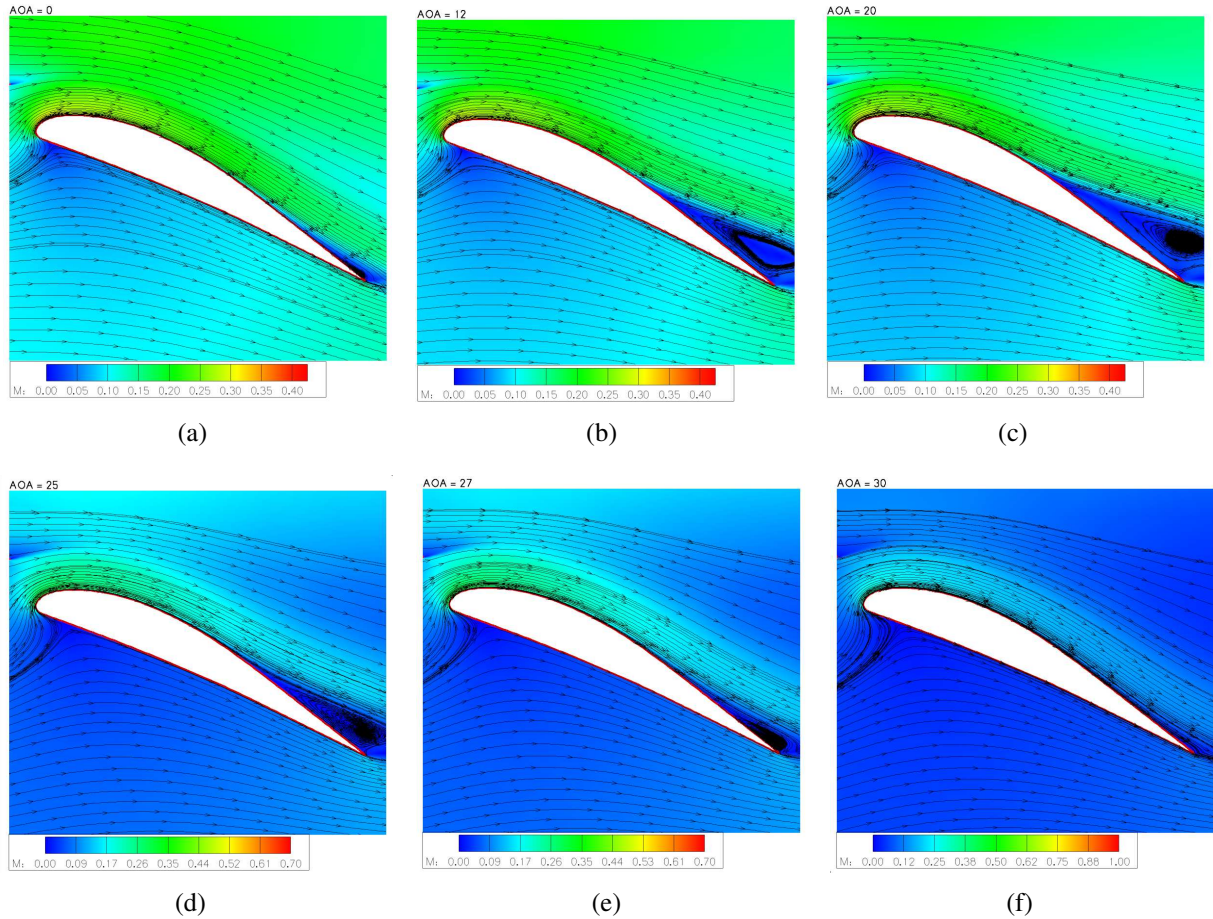


Fig. 15 Flow pattern over the flap of optimum configuration obtained with parametric study of flap position.

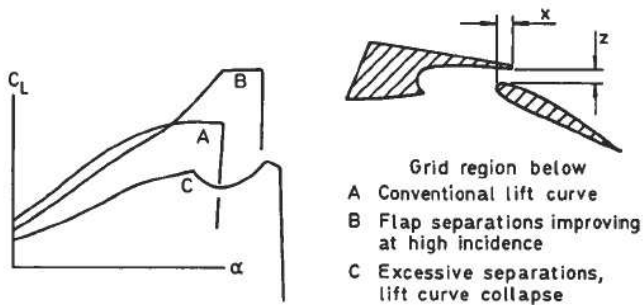


Fig. 16 The three types of aerodynamic design for the high-lift devices.

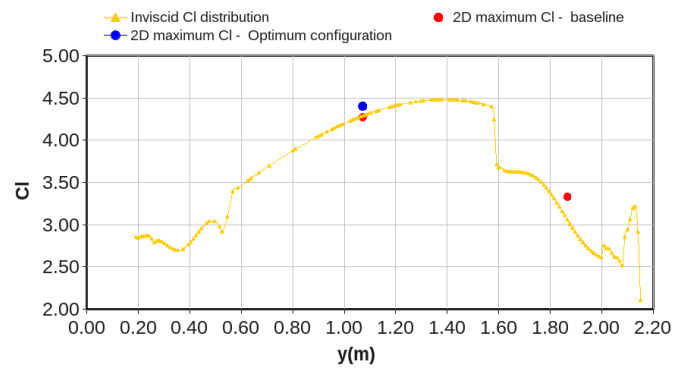


Fig. 17 Wing loading distribution and maximum local at two wing stations to define the  $CL_{max}$ .

$C_{L_{max}}$ , considering the correction factor, for the baseline and the optimum configurations are 2.51 and 2.58, respectively. The methodology yields an improvement in  $C_{L_{max}}$  of 0.07, which is not in accordance with the three-dimensional results.

## 7 Three-Dimensional Analysis

In this section of the present work, the three-dimensional results, obtained for the optimum

configuration from the parametric study, is presented. Figure 18 shows the  $C_L$  versus angle of attack curve for the baseline and the optimum configuration. It is possible to observe that the three-dimensional results behave similarly to those obtained for the two-dimensional analysis, as indicated in Figs. 10 and 12, in the sense that the optimization for a high angle of attack yields a reduction in the lift coefficient at zero angle of attack,  $C_{L_0}$ . The increase in the maximum lift

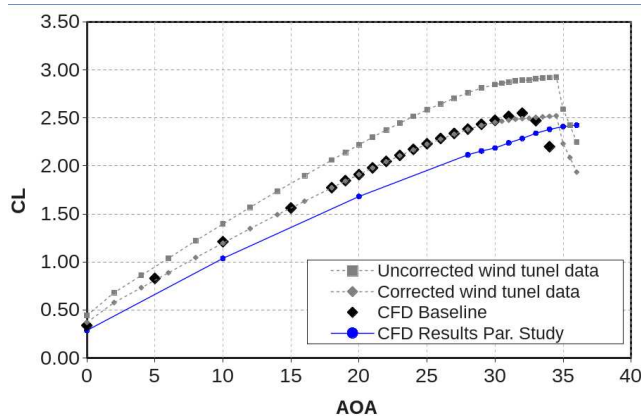


**Fig. 18** Comparison between the experimental for baseline configuration and the numerical results for baseline and optimum configuration via obtained parametric study.

coefficient is not observed up to the last evaluated angle of attack. A very reasonable explanation for this behavior lies on the fact that the best displacement for the mid-span section of the flap panel might be degenerating the most outboard section of the flap panel. This most outboard part of the flap panel is the one that has the highest aerodynamic loading and the imposed displacement yields a separated flow condition in the most outboard panel that does not recover even at higher angles of attack as can be observed in Figs. 19 and 20. The important point here is that the two-dimensional optimization must be performed for more than one section, as it is practice in industry.

Figure 19 shows the top view of pressure contours, superimposed upon the shear lines, for the optimum and the baseline configurations at

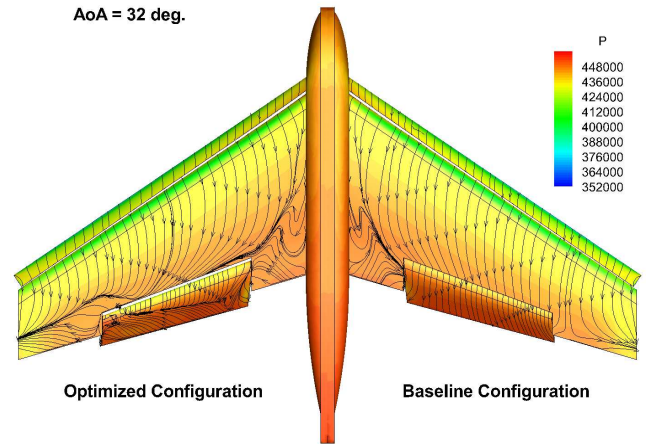


**Fig. 19** Pattern of surface shear stress lines due to flow around baseline and optimized, via parametric study, configurations.

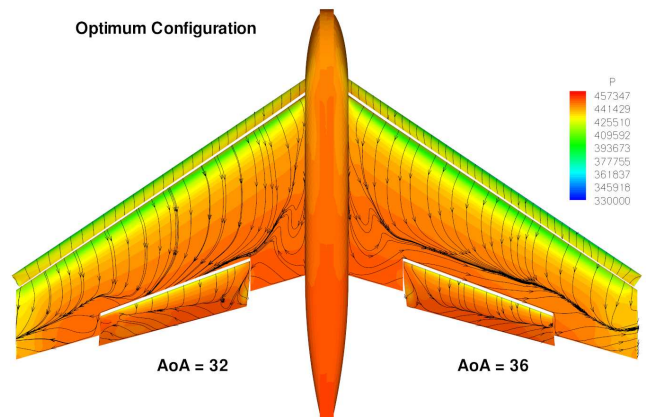


**Fig. 20** Pattern of surface shear stress lines for the configuration optimized via parametric study.

$\alpha = 32$  deg., which is the angle of attack for maximum lift for the baseline configuration. It is possible to observe that the optimized configuration has a sizeable region of separated flow over its flap panel at this angle of attack. However, observation of Fig. 18 seems to indicate that the optimized wing has not reached maximum lift at  $\alpha = 32$  deg. Therefore, if one continues to increase the angle of attack, the separated region in the flap of the optimized configuration tends to decrease, hence further increasing the overall lift of the configuration. This is corroborated by the results shown in Fig. 20, which clearly indicate a

reduction in the flow separation over the flap for  $\alpha = 36$  deg.

## 8 Concluding Remarks

The present work has shown an optimization strategy that is successful in yielding improvements in the maximum lift coefficient of a high-lift device. The use of the mesh morphing methodology has shown to be a very helpful approach to minimize the computational cost of having to generate the mesh for every proposed configuration. The semi-empirical methodology has shown to be able to capture some effect of the increase in the wing  $C_{L_{\max}}$  due to improvements in the local (2-D) maximum lift coefficient from the mid-span section. The 3-D results seem to indicate an increase in the angle of attack for maximum lift.

Some of the differences between the 2-D and 3-D results can be attributed to the effects that emerge from the geometrical discontinuity at the flat edges, which are not contemplated in the 2-D analysis. In order to minimize such effects, it is recommended to consider more than one station during the 2-D design process.

## Acknowledgments

The authors gratefully acknowledge the partial support for this research provided by Conselho Nacional de Desenvolvimento Científico e Tecnológico, CNPq, under the Research Grant No. 309985/2013-7. This work is also supported by Fundação de Amparo à Pesquisa do Estado de São Paulo, FAPESP, under Grant No. 2013/07375-0.

## References

- [1] van Dam, C.P., “The Aerodynamic Design of Multi-Element High-Lift Systems for Transport Airplanes,” *Progress in Aerospace Sciences*, Vol. 38, No. 2, Feb. 2002, pp. 101-114.
- [2] Chaffin, M., and Pirzadeh, S., “Unstructured Navier-Stokes High-Lift Computations on a Trapezoidal Wing,” AIAA Paper No. 2005-5084, *Proceedings of the 23rd AIAA Applied*

*Aerodynamics Conference*, Toronto, Canada, Jun. 2005.

- [3] Johnson, P., Jones, K.M., and Madson, M., “Experimental Investigation of a Simplified 3D High-Lift Configuration in Support of CFD Validation,” AIAA Paper No. 2000-4217, *Proceedings of the 18th AIAA Applied Aerodynamics Conference and Exhibit*, Denver, CO, Aug. 2000.
- [4] ICFM-CFD™, <http://www.icemcfd.com/>.
- [5] Spalart, P.R., and Allmaras, S.R., “A One-Equation Turbulence Model for Aerodynamic Flows,” AIAA Paper No. 92-0439, *30th AIAA Aerospace Sciences Meeting and Exhibit*, Reno, NV, Jan. 1992.
- [6] Metacomp Technologies Inc., CFD++, <http://www.metacomptech.com/>.
- [7] Mode-Frontier, <http://www.esteco.com/>.
- [8] Sasaki, D., “ARMOGA an Efficient Multi-Objective Genetic Algorithm,” Esteco Inc., Mode-Frontier, 2005.
- [9] Smith, A. M. O., “High-Lift Aerodynamics,” *J. Aircraft*, Vol. 12, No. 6, Jun. 1975, pp. 501-530.
- [10] Woodward, D. S., and Lean, D. E., “Where is High-Lift Today? A Review of Past UK Research Programmes,” *High-Lift Systems Aerodynamics*, AGARD-CP-515, Sept. 1993.

## 9 Contact Author Email Address

R. G. Silva, [ri\\_galdino@yahoo.com.br](mailto:ri_galdino@yahoo.com.br)  
 A. P. Antunes, [alexandre.antunes@embraer.com.br](mailto:alexandre.antunes@embraer.com.br)  
 R. B. Flatschart, [ricardo.flatschart@embraer.com.br](mailto:ricardo.flatschart@embraer.com.br)  
 J. L. F. Azevedo, [joaoluiz.azevedo@gmail.com](mailto:joaoluiz.azevedo@gmail.com)

## Copyright Statement

The authors confirm that they, and/or their company or organization, hold copyright on all of the original material included in this paper. The authors also confirm that they have obtained permission, from the copyright holder of any third party material included in this paper, to publish it as part of their paper. The authors confirm that they give permission, or have obtained permission from the copyright holder of this paper, for the publication and distribution of this paper as part of the ICAS2014 proceedings or as individual off-prints from the proceedings.